

# Energy-Conserving Data-Driven Discretizations for Maxwell's Equations

Victory C. Obieke

Department of Mathematics, Oregon State University  
 obiekev@oregonstate.edu

## Abstract

We study data-driven construction of spatial discretizations for the one-dimensional Maxwell system. Given high-fidelity training data generated by a spectral discretization, we learn a *linear convolution stencil* that approximates the spatial derivative operator appearing in Maxwell's equations. The stencil is obtained by solving a convex quadratic optimization problem, subject to linear constraints that enforce skew-adjointness of the discrete derivative. These constraints guarantee a semi-discrete energy identity for the resulting Maxwell system. We prove that our constraints characterize the class of skew-symmetric convolution operators and express the associated numerical wave speed and CFL restriction for the classical leapfrog scheme in terms of the learned stencil's Fourier symbol. We then compare several convex solvers for the resulting quadratic program—projected gradient, Nesterov-accelerated gradient, ADMM, and an interior-point reference implemented in CVXPY—and evaluate the learned schemes in time-dependent one-dimensional Maxwell simulations using a Crank–Nicolson (CN) time discretization. Our numerical experiments show that (i) energy-constrained learned stencils achieve accuracy comparable to standard central differences while exactly preserving the discrete electromagnetic energy under CN time-stepping, and (ii) ADMM and interior-point methods produce nearly identical operators, with ADMM offering a favorable tradeoff between accuracy, constraint satisfaction, and runtime.

## 1 Introduction

Finite-difference time-domain (FDTD) methods are a standard tool for solving Maxwell's equations in computational electromagnetics [15]. Classical schemes, such as the Yee method, are derived by hand from the continuous equations, with spatial derivatives approximated using fixed central-difference stencils and stability enforced via analytical CFL conditions. Recently, there has been growing interest in *data-driven discretizations*, where discrete operators are learned from numerical or experimental data, e.g., via regression or neural networks. Examples include data-driven discretization of Burgers and Navier–Stokes equations and learned coarse-grid operators for PDEs [1].

Most existing data-driven schemes aim to minimize approximation error but do not explicitly enforce structural properties such as stability, conservation, or energy balance. For Maxwell's equations this is a significant limitation, since standard FDTD schemes are carefully designed so that discrete versions of divergence constraints and energy identities hold at the semi-discrete level.

In this work we address this gap in a simple but concrete setting: the one-dimensional TE Maxwell system with periodic boundary conditions. Our goal is to learn a discrete spatial derivative operator

$$D : \mathbb{R}^N \rightarrow \mathbb{R}^N$$

represented as a convolution stencil, directly from data. We impose linear constraints on the stencil that enforce *skew-adjointness* of  $D$  with respect to the discrete  $L^2$  inner product. This structural constraint guarantees exact conservation of discrete electromagnetic energy at the semi-discrete level, regardless of the details of the training data.

**Novelty and contributions.** Building on this context, our main contributions are as follows:

- We formulate a convex quadratic optimization problem for learning convolution stencils for the 1D Maxwell system from spectral training data. The objective is a least-squares misfit between the learned discrete derivative and high-fidelity derivatives, while the constraints encode skew-symmetry of the stencil coefficients together with simple box bounds.
- We show that these linear constraints are *exactly* equivalent to skew-adjointness of the corresponding convolution operator with respect to the discrete  $L^2$  inner product, and hence to a semi-discrete electromagnetic energy identity. This yields, to our knowledge, the first learned Maxwell stencil with a *guaranteed* semi-discrete energy conservation law.
- We characterize the numerical wave speed and associated CFL restriction of the learned discrete curl operator purely in terms of its Fourier symbol  $\mu(\theta)$ .
- We implement projected gradient, Nesterov-accelerated gradient, ADMM, and an interior-point method (via CVXPY) to solve the constrained quadratic program, and we benchmark the resulting stencils in time-dependent 1D Maxwell simulations. The experiments compare PDE error, energy-constraint residuals, and energy evolution across stencil radii, and demonstrate that ADMM and interior-point methods produce nearly identical, highly accurate stencils, with ADMM offering a favorable tradeoff between accuracy, constraint satisfaction, and runtime.

Although our experiments focus on a simple 1D periodic model, the framework and energy constraints extend naturally to higher-dimensional settings and more complex material models.

Our results illustrate how even simple linear constraints in a data-driven discretization can encode important physics and restore structural properties such as energy conservation.

## 1.1 Related work

**Data-driven discretizations.** There is a growing literature on learning discretizations and coarse-grid operators for PDEs directly from data. A prominent example is the work of [1], who learn finite-difference schemes for Burgers and Navier–Stokes equations by fitting local stencils to high-fidelity solutions while optimizing accuracy on a training set. Related approaches use regression or neural networks to construct reduced models or learned fluxes for time-dependent PDEs; see, e.g., [11, 9, 14, 12, 7]. In most of these methods, the learned operators are chosen solely to minimize an empirical error measure and are not required to satisfy structural constraints such as conservation, stability, or symmetries of the underlying PDE. In contrast, our focus is on learning a discrete Maxwell operator that *provably* satisfies a semi-discrete energy identity through an explicit skew-adjointness constraint on the convolution stencil.

**Energy-preserving FDTD and skew-adjoint schemes.** Classical finite-difference time-domain (FDTD) methods for Maxwell’s equations, such as the Yee scheme and its variants, are carefully constructed so that discrete versions of divergence constraints and energy identities hold at the semi-discrete or fully discrete level [15, 13, 10, 8]. In particular, staggered spatial discretizations

and symplectic or A-stable time integrators such as the Crank–Nicolson scheme are often used to obtain skew-adjoint or nearly skew-adjoint update operators, leading to strong stability and conservation properties [3, 4, 6]. There is also a large body of work on structure-preserving and geometric integrators for Hamiltonian ODE/PDE systems, which emphasizes invariants such as energy and symplectic form [5]. Our work is closest in spirit to these structure-preserving schemes, but differs in that the discrete spatial operator is *learned* from data rather than hand-designed: we encode skew-adjointness as a set of linear constraints on the stencil coefficients and solve a convex quadratic program to obtain an energy-conserving discretization.

**This work in context.** To the best of our knowledge, the present paper is the first to combine data-driven stencil learning for Maxwell’s equations with linear constraints that (i) exactly characterize skew-symmetric convolution operators and (ii) yield a rigorous semi-discrete energy identity and a CFL condition expressed directly in terms of the learned stencil’s Fourier symbol. This provides a bridge between unconstrained data-driven discretizations and classical energy-preserving FDTD schemes, while remaining compatible with standard convex optimization toolchains (projected gradient, Nesterov acceleration, ADMM, and interior-point solvers).

## 2 Semi-discrete Maxwell system and energy identity

We consider the 1D Maxwell system in vacuum, written in non-dimensional form with  $\varepsilon_0 = \mu_0 = 1$ :

$$\partial_t E = \partial_x H, \quad \partial_t H = \partial_x E, \quad (1)$$

on the periodic domain  $[0, L]$ .

We discretize space using a uniform grid  $x_i = i\Delta x$ ,  $i = 0, \dots, N - 1$ , with  $\Delta x = L/N$ , and collect the nodal values of the electric and magnetic fields into vectors

$$\mathbf{E}(t) = (E_0(t), \dots, E_{N-1}(t))^\top, \quad \mathbf{H}(t) = (H_0(t), \dots, H_{N-1}(t))^\top.$$

Let  $D : \mathbb{R}^N \rightarrow \mathbb{R}^N$  denote a linear discrete derivative operator. In this work,  $D$  is a *convolution operator* defined by a stencil  $w \in \mathbb{R}^{2R+1}$ ,

$$(D\mathbf{u})_i = \sum_{\ell=-R}^R w_\ell u_{i+\ell}, \quad i = 0, \dots, N - 1, \quad (2)$$

with periodic wrap-around in the index  $i + \ell$ . The semi-discrete Maxwell system then reads

$$\frac{d}{dt} \mathbf{E}(t) = D\mathbf{H}(t), \quad \frac{d}{dt} \mathbf{H}(t) = D\mathbf{E}(t). \quad (3)$$

We equip  $\mathbb{R}^N$  with the standard discrete  $L^2$  inner product

$$\langle \mathbf{u}, \mathbf{v} \rangle := \Delta x \sum_{i=0}^{N-1} u_i v_i, \quad \|\mathbf{u}\|^2 := \langle \mathbf{u}, \mathbf{u} \rangle. \quad (4)$$

The corresponding discrete electromagnetic energy is

$$\mathcal{E}(t) := \frac{1}{2} \|\mathbf{E}(t)\|^2 + \frac{1}{2} \|\mathbf{H}(t)\|^2. \quad (5)$$

**Theorem 1** (Semi-discrete energy identity). *Let  $D$  be any linear operator on  $\mathbb{R}^N$ , and let  $\mathbf{E}(t), \mathbf{H}(t)$  satisfy (3). Then*

$$\frac{d}{dt}\mathcal{E}(t) = \langle D\mathbf{H}(t), \mathbf{E}(t) \rangle + \langle D\mathbf{E}(t), \mathbf{H}(t) \rangle. \quad (6)$$

*In particular, if  $D$  is skew-adjoint with respect to (4), i.e.,*

$$\langle D\mathbf{u}, \mathbf{v} \rangle = -\langle \mathbf{u}, D\mathbf{v} \rangle \quad \forall \mathbf{u}, \mathbf{v}, \quad (7)$$

*then the discrete energy is exactly conserved:*

$$\frac{d}{dt}\mathcal{E}(t) = 0. \quad (8)$$

*Proof.* Differentiating (5) in time and using (3) gives

$$\begin{aligned} \frac{d}{dt}\mathcal{E}(t) &= \left\langle \frac{d}{dt}\mathbf{E}(t), \mathbf{E}(t) \right\rangle + \left\langle \frac{d}{dt}\mathbf{H}(t), \mathbf{H}(t) \right\rangle \\ &= \langle D\mathbf{H}(t), \mathbf{E}(t) \rangle + \langle D\mathbf{E}(t), \mathbf{H}(t) \rangle, \end{aligned}$$

which is (6). If  $D$  is skew-adjoint, then

$$\langle D\mathbf{H}, \mathbf{E} \rangle = -\langle \mathbf{H}, D\mathbf{E} \rangle = -\langle D\mathbf{E}, \mathbf{H} \rangle,$$

so the two terms in (6) cancel and  $\frac{d}{dt}\mathcal{E}(t) = 0$ .  $\square$

## 2.1 Skew-symmetric convolution operators and stencil constraints

We now specialize to convolution operators of the form (2) with periodic boundary conditions. Let  $w = (w_{-R}, \dots, w_{-1}, w_0, w_1, \dots, w_R)^\top$  be the stencil.

**Lemma 1.** *Let  $D$  be defined by (2) with periodic wrap-around. Then the matrix entries of  $D$  satisfy*

$$D_{ij} = w_{i-j}, \quad i, j = 0, \dots, N-1, \quad (9)$$

*where the difference  $i - j$  is taken modulo  $N$ .*

*Proof.* By definition,

$$(D\mathbf{u})_i = \sum_{\ell=-R}^R w_\ell u_{i+\ell} = \sum_{j=0}^{N-1} w_{i-j} u_j,$$

where  $j = i + \ell$  (modulo  $N$ ). Hence  $D_{ij} = w_{i-j}$ .  $\square$

**Theorem 2** (Characterization of skew-symmetric stencils). *[2] Let  $D$  be the convolution operator (2) with periodic boundary conditions and stencil  $w \in \mathbb{R}^{2R+1}$ . Then  $D$  is skew-adjoint with respect to (4), i.e.,  $D^\top = -D$ , if and only if the stencil satisfies*

$$w_0 = 0, \quad w_{-\ell} = -w_{+\ell}, \quad \ell = 1, \dots, R. \quad (10)$$

*Proof.* By Lemma 1 the entries of  $D$  are  $D_{ij} = w_{i-j}$ , so

$$(D^\top)_{ij} = D_{ji} = w_{j-i}.$$

The condition  $D^\top = -D$  is therefore equivalent to

$$w_{j-i} = -w_{i-j} \quad \text{for all } i, j,$$

or, writing  $\ell = i - j$ ,

$$w_{-\ell} = -w_{+\ell} \quad \text{for all } \ell.$$

In particular, taking  $\ell = 0$  yields  $w_0 = -w_0$ , hence  $w_0 = 0$ , and for  $\ell = 1, \dots, R$  we obtain  $w_{-\ell} = -w_{+\ell}$ . Conversely, if (10) holds, then the above computation shows  $D^\top = -D$ , i.e.,  $D$  is skew-adjoint.  $\square$

We encode the conditions (10) as a set of linear constraints on the stencil vector  $w$ . Let  $C \in \mathbb{R}^{(R+1) \times (2R+1)}$  be defined by

$$(Cw)_0 = w_0, \quad (Cw)_\ell = w_{-\ell} + w_{+\ell}, \quad \ell = 1, \dots, R,$$

and let  $d \in \mathbb{R}^{R+1}$  be the zero vector. Then the constraint  $Cw = d$  is simply

$$w_0 = 0, \quad w_{-\ell} + w_{+\ell} = 0, \quad \ell = 1, \dots, R, \quad (11)$$

which is equivalent to skew-symmetry.

**Corollary 1.** *Let  $C$  and  $d$  be defined in (11). Then  $Cw = d$  if and only if the stencil  $w$  satisfies (10), i.e., if and only if the corresponding convolution operator  $D$  is skew-adjoint.*

*Proof.* Immediate from (11) and Theorem 2.  $\square$

Corollary 1 shows that the linear constraint  $Cw = d$  used in our optimization problem is *exactly* the condition required for semi-discrete energy conservation via Theorem 1.

### 3 Wave speed and CFL for the learned operator

The discrete curl operator  $D$  constructed in Section 2.1 is a periodic convolution with stencil  $w = (w_{-R}, \dots, w_0, \dots, w_R)$  satisfying the skew-symmetry constraints of Theorem 2. For such an operator it is convenient to work with its Fourier symbol

$$\mu(\theta) := \sum_{k=-R}^R w_k e^{ik\theta}, \quad \theta \in [-\pi, \pi], \quad (12)$$

which characterizes the response of  $D$  to discrete Fourier modes  $e^{ij\theta}$ .

For the semi-discrete Maxwell system

$$\frac{d}{dt} \begin{bmatrix} \mathbf{H} \\ \mathbf{E} \end{bmatrix} = A \begin{bmatrix} \mathbf{H} \\ \mathbf{E} \end{bmatrix}, \quad A = \begin{bmatrix} 0 & D \\ D^T & 0 \end{bmatrix},$$

the eigenvalues of  $A$  are purely imaginary and can be written as  $\lambda(\theta) = \pm i |\mu(\theta)|$  for  $\theta \in [-\pi, \pi]$ . In particular, the quantity  $|\mu(\theta)|$  plays the role of a *numerical wave speed* for the mode  $\theta$ , and the maximal value

$$c_{\max} := \max_{\theta \in [-\pi, \pi]} |\mu(\theta)| \quad (13)$$

is the largest speed supported by the learned operator. For the standard centered difference stencil of width three one recovers  $c_{\max} \sim h^{-1}$ , corresponding to the usual CFL restriction for explicit wave propagation schemes.

If one were to apply the classical leapfrog scheme to the semi-discrete system, stability of the scalar test equation  $\dot{u} = \lambda u$  with  $\lambda = i\omega$  requires  $\Delta t |\omega| \leq 2$ , see, e.g., [13, 10, 8]. Substituting  $\omega = \pm|\mu(\theta)|$  and maximizing over  $\theta$  yields the CFL condition

$$\Delta t \leq \frac{2}{c_{\max}}, \quad (14)$$

which expresses the admissible time step solely in terms of the learned symbol (12). In this way the learned stencil can be interpreted within the familiar CFL framework for explicit FDTD schemes, although in our numerical experiments we will use an implicit time integrator.

### 3.1 Crank–Nicolson time integration

For the actual time-dependent simulations in Section 6 we use the Crank–Nicolson (CN) method applied to the semi-discrete system

$$\frac{d\mathbf{U}}{dt} = A\mathbf{U}, \quad \mathbf{U} = \begin{bmatrix} \mathbf{H} \\ \mathbf{E} \end{bmatrix}, \quad A^T = -A.$$

The CN update reads

$$\frac{\mathbf{U}^{n+1} - \mathbf{U}^n}{\Delta t} = A \frac{\mathbf{U}^{n+1} + \mathbf{U}^n}{2}, \quad (15)$$

which coincides with the implicit midpoint rule for linear systems. Since  $A$  is skew-adjoint, the discrete energy

$$\mathcal{E}^n := \frac{1}{2} \|\mathbf{U}^n\|_2^2 = \frac{1}{2} (\|\mathbf{H}^n\|_2^2 + \|\mathbf{E}^n\|_2^2)$$

is preserved exactly by (15) for any time step  $\Delta t > 0$ ; see, e.g., [5, 6] for background on such structure-preserving schemes.

In particular, CN does not require the CFL restriction (14) for stability or energy conservation in this linear, skew-adjoint setting. In the numerical experiments we nevertheless choose a time step  $\Delta t$  proportional to the grid spacing  $h$  and small enough that (14) would be satisfied for the corresponding centered-difference operator. This ensures that temporal discretization errors remain small relative to the spatial error while allowing us to interpret the learned stencil in terms of an effective wave speed  $c_{\max}$ .

## 4 Data-driven stencil learning

We now formulate the quadratic optimization problem used to learn stencils from data generated by a high-fidelity discretization.

### 4.1 Training data from spectral 1D Maxwell

We generate training data by sampling random Maxwell states and computing their time derivatives exactly (up to spectral discretization error). We work on the periodic domain  $[0, L]$  with  $N$  grid

points and spacing  $\Delta x = L/N$ . For each training sample we draw a random truncated Fourier series

$$E(x) = \sum_{m=1}^{m_{\max}} a_m \sin\left(\frac{2\pi mx}{L} + \phi_m\right),$$

$$H(x) = \sum_{m=1}^{m_{\max}} b_m \sin\left(\frac{2\pi mx}{L} + \psi_m\right),$$

with amplitudes  $a_m, b_m$  and phases  $\phi_m, \psi_m$  drawn from simple Gaussian and uniform distributions. We then compute the spatial derivatives  $\partial_x E$  and  $\partial_x H$  spectrally using FFTs:

$$\partial_x E = \mathcal{F}^{-1}\left(\text{i}k \hat{E}\right), \quad \partial_x H = \mathcal{F}^{-1}\left(\text{i}k \hat{H}\right),$$

where  $k$  is the discrete wavenumber. Finally, we obtain the time derivatives from the PDE (1):

$$\partial_t E = \partial_x H, \quad \partial_t H = \partial_x E.$$

We denote by

$$U \in \mathbb{R}^{n_{\text{sims}} \times 2 \times N}$$

the array of training states, where  $U[s, 0, i] = E^{(s)}(x_i)$  and  $U[s, 1, i] = H^{(s)}(x_i)$  denote the electric and magnetic fields of the  $s$ -th training sample evaluated at the grid point  $x_i$ . Similarly,

$$\frac{dU}{dt} \in \mathbb{R}^{n_{\text{sims}} \times 2 \times N}$$

stores the corresponding time derivatives, with  $(dU/dt)[s, 0, i] = \partial_t E^{(s)}(x_i)$  and  $(dU/dt)[s, 1, i] = \partial_t H^{(s)}(x_i)$ .

Here  $n_{\text{sims}}$  denotes the number of independent training samples (or snapshots), each consisting of a randomly generated Maxwell state  $(E, H)$  and its corresponding time derivative. The spatial domain  $[0, L]$  is discretized using  $N$  uniformly spaced grid points  $x_i = i\Delta x$ ,  $i = 0, \dots, N-1$ , where  $\Delta x = L/N$ .

## 4.2 Least-squares formulation

Given training pairs  $(\mathbf{E}, \mathbf{H})$  and  $(\partial_t \mathbf{E}, \partial_t \mathbf{H})$ , we wish to learn a single convolution stencil  $w$  such that

$$D\mathbf{H} \approx \partial_x \mathbf{H} = \partial_t \mathbf{E}, \quad D\mathbf{E} \approx \partial_x \mathbf{E} = \partial_t \mathbf{H},$$

in a least-squares sense. For each grid index  $i$  away from the boundaries we extract local patches

$$\mathbf{h}_i = (H_{i-R}, \dots, H_{i+R})^\top, \quad \mathbf{e}_i = (E_{i-R}, \dots, E_{i+R})^\top,$$

and define scalar targets

$$y_i^{(H)} = \partial_t E_i, \quad y_i^{(E)} = \partial_t H_i.$$

The desired relationships are

$$w^\top \mathbf{h}_i \approx y_i^{(H)}, \quad w^\top \mathbf{e}_i \approx y_i^{(E)}.$$

Stacking all patches and targets over space and all simulations, we obtain a linear system

$$Aw \approx b, \tag{16}$$

where each row of  $A$  is either  $\mathbf{h}_i^\top$  or  $\mathbf{e}_i^\top$ , and  $b$  collects the corresponding targets. This leads to the unconstrained least-squares problem

$$\min_{w \in \mathbb{R}^{2R+1}} \frac{1}{2} \|Aw - b\|_2^2 + \frac{\lambda}{2} \|w\|_2^2, \quad (17)$$

where  $\lambda \geq 0$  is a small Tikhonov regularization parameter.

### 4.3 Energy constraint and box bounds

To enforce skew-adjointness and hence discrete energy conservation, we impose the linear constraint  $Cw = d$  with  $C$  and  $d$  defined as in Section 2.1. By Corollary 1, any stencil satisfying  $Cw = d$  defines a skew-adjoint convolution operator  $D$  and therefore an energy-conserving semi-discrete Maxwell system.

We also impose simple box bounds  $|w_\ell| \leq M$ , i.e.,

$$-M \leq w_\ell \leq M, \quad \ell = -R, \dots, R, \quad (18)$$

where  $M > 0$  is chosen large enough to contain the true derivative stencil but small enough to control numerical conditioning.

Our final optimization problem is the convex quadratic program

$$\begin{aligned} \min_{w \in \mathbb{R}^{2R+1}} \quad & \frac{1}{2} \|Aw - b\|_2^2 + \frac{\lambda}{2} \|w\|_2^2, \\ \text{s.t.} \quad & Cw = d, \\ & -M \leq w \leq M. \end{aligned} \quad (19)$$

This problem is strictly convex for  $\lambda > 0$  and admits a unique solution. For our first-order methods we use a slightly simplified variant of (19) in which only the linear energy constraint is enforced. Specifically, projected gradient (PG) and Nesterov-accelerated gradient (NAG) are applied to the equality-constrained problem

$$\begin{aligned} \min_{w \in \mathbb{R}^{2R+1}} \quad & \frac{1}{2} \|Aw - b\|_2^2 + \frac{\lambda}{2} \|w\|_2^2, \\ \text{s.t.} \quad & Cw = d, \end{aligned} \quad (20)$$

while the full equality-plus-box-constrained problem (19) is handled by ADMM and the interior-point solver in CVXPY. In our experiments the solutions of (20) produced by PG and NAG remain well inside the box  $[-M, M]^{2R+1}$ , so the difference between (20) and (19) is negligible in practice.

## 5 Convex solvers

We briefly summarize the algorithms used to solve (19). All methods operate on the same design matrix  $A$ , constraint matrix  $C$ , and bounds.

### 5.1 Projected gradient methods

Our first two solvers are projected gradient (PG) and Nesterov-accelerated gradient (NAG), applied to the *equality-constrained* problem (20). In particular, for PG/NAG we enforce only the linear energy constraint  $Cw = d$  and do not explicitly impose the box bounds  $-M \leq w \leq M$ . In our

experiments the PG/NAG iterates remain strictly inside the box, so the resulting solutions agree (to numerical tolerance) with those of the fully constrained problem (19).

Define the feasible affine subspace

$$\mathcal{C}_{\text{eq}} = \{w \in \mathbb{R}^{2R+1} : Cw = d\}.$$

The orthogonal projection onto  $\mathcal{C}_{\text{eq}}$  with respect to the Euclidean inner product is given explicitly by

$$P_{\mathcal{C}_{\text{eq}}}(z) := z - C^\top (CC^\top)^{-1}(Cz - d), \quad z \in \mathbb{R}^{2R+1}, \quad (21)$$

assuming that  $C$  has full row rank.

Let

$$f(w) := \frac{1}{2}\|Aw - b\|_2^2 + \frac{\lambda}{2}\|w\|_2^2, \quad \nabla f(w) = A^\top(Aw - b) + \lambda w.$$

We choose a stepsize  $\alpha = 1/L$ , where one may take  $L = \|A\|_2^2 + \lambda = \|A^\top A\|_2 + \lambda$ .

For PG, the update is

$$w^{k+1} = P_{\mathcal{C}_{\text{eq}}}\left(w^k - \alpha \nabla f(w^k)\right),$$

with  $P_{\mathcal{C}_{\text{eq}}}$  given by (21).

For NAG we use the extrapolated point

$$y^k = w^k + \beta_k(w^k - w^{k-1}),$$

and then update

$$w^{k+1} = P_{\mathcal{C}_{\text{eq}}}\left(y^k - \alpha \nabla f(y^k)\right),$$

with the standard parameters

$$t_{k+1} = \frac{1}{2}\left(1 + \sqrt{1 + 4t_k^2}\right), \quad \beta_k = \frac{t_k - 1}{t_{k+1}}, \quad t_0 = 1.$$

We track the objective  $f(w^k)$ , wall-clock time, and the equality residual  $\|Cw^k - d\|_2$  at each iteration.

**Remark 1.** *Projecting sequentially onto  $\{Cw = d\}$  and the box  $[-M, M]^{2R+1}$  is not, in general, the exact Euclidean projection onto their intersection. If the box constraint becomes active and one wishes to enforce both constraints within a projected-gradient framework, one should compute  $P_{\{Cw=d\} \cap [-M, M]^{2R+1}}$  using an intersection projection method such as Dykstra's algorithm, or solve the projection step as a small quadratic program.*

## 5.2 ADMM

To better handle the combination of equality and box constraints, we also implement an alternating direction method of multipliers (ADMM) scheme. We introduce a copy  $z$  of  $w$  and enforce the box constraint on  $z$  only:

$$w \in \mathbb{R}^{2R+1}, \quad z \in [-M, M]^{2R+1}, \quad w = z, \quad Cw = d.$$

The augmented Lagrangian splits into a quadratic  $w$ -problem with equality constraints and a simple proximal  $z$ -update given by box projection. The  $w$ -update reduces to solving a KKT system of the form

$$\begin{bmatrix} A^\top A + (\lambda + \rho)I & C^\top \\ C & 0 \end{bmatrix} \begin{bmatrix} w \\ \eta \end{bmatrix} = \begin{bmatrix} A^\top b + \rho(z - u) \\ d \end{bmatrix},$$

where  $\rho > 0$  is the ADMM penalty parameter and  $\eta$  is a vector of Lagrange multipliers for the equality constraints. The  $z$ -update is just componentwise clipping,  $z^{k+1} = \Pi_{[-M, M]^{2R+1}}(w^{k+1} + u^k)$ , and the dual update is  $u^{k+1} = u^k + (w^{k+1} - z^{k+1})$ . We again monitor the objective, equality residual, and primal difference  $\|w^{k+1} - w^k\|$ .

### 5.3 Interior-point reference (CVXPY)

Finally, we use the CVXPY modeling framework with a cone solver (SCS in our experiments) to obtain a reference solution to (19). This interior-point-based solution serves as a baseline for the quality of the first-order methods. The corresponding routine `solve_cvx` sets up the quadratic objective and linear constraints, and returns the optimal stencil  $w_{\text{cvx}}$  when CVXPY is available.

## 6 Numerical experiments

We now present numerical experiments in the 1D Maxwell setting to evaluate the learned stencils and the performance of the different solvers. All experiments use the Crank–Nicolson (CN) time integrator with the learned spatial operator.

### 6.1 Experimental setup

Unless otherwise stated, we use the following default parameters:

- Spatial domain  $[0, L]$  with  $L = 1$  and  $N = 64$  cells,  $\Delta x = L/N$ .
- Training data:  $n_{\text{sims}} = 200$  random spectral samples with  $m_{\text{max}} = 5$  Fourier modes.
- Regularization parameter  $\lambda = 10^{-6}$  and box parameter  $M = 100$ .
- Stencil radii  $R \in \{1, 2, 3, 4\}$ , corresponding to stencil length  $2R + 1$ .
- Time integration: Crank–Nicolson (CN) applied to the semi-discrete system with time step  $\Delta t = 0.5\Delta x$  and  $N_t = 300$  time steps.

The initial condition for time integration is chosen as a single Fourier mode,

$$E(x, 0) = \sin(2\pi x/L), \quad H(x, 0) = \cos(2\pi x/L),$$

and we compute a reference solution using the exact central-difference stencil

$$w_{\text{exact}} = \frac{1}{2\Delta x}(-1, 0, 1), \quad (22)$$

We then integrate the Maxwell system with each learned stencil using CN and measure the relative  $L^2$  error in the electric field at final time:

$$\text{err}(w) = \frac{\|\mathbf{E}^{\text{learned}}(T) - \mathbf{E}^{\text{FD}}(T)\|_2}{\|\mathbf{E}^{\text{FD}}(T)\|_2}. \quad (23)$$

We also compute the energy-constraint residual

$$r_{\text{eq}}(w) = \|Cw - d\|_2,$$

which is zero for an exactly skew-symmetric stencil.

As an additional diagnostic, we track the discrete electromagnetic energy

$$\mathcal{E}^n := \frac{1}{2} \Delta x \sum_i [(E_i^n)^2 + (H_i^n)^2]$$

over time. For the exact stencil and CN time-stepping, the code confirms that  $\mathcal{E}^n$  is constant to within floating-point roundoff, consistent with the analysis in Section 2.

## 6.2 Learned stencils for $R = 1$

For  $R = 1$  the true centered-difference stencil is precisely  $w_{\text{exact}}$  from (22).

Table 1 shows the learned stencils obtained by each solver compared with  $w_{\text{exact}}$ . We observe that all methods recover a stencil very close to the exact one, with small differences due to the finite training set and regularization.

Method	$w_{-1}$	$w_0$	$w_{+1}$
Exact FD	-32.000000	0.000000	32.000000
PG	-32.906110	0.000000	32.906110
NAG	-32.906098	0.000000	32.906098
ADMM	-32.906114	$-2.64 \times 10^{-16}$	32.906114
CVX	-32.906115	$-1.57 \times 10^{-14}$	32.906115

Table 1: Learned stencils for radius  $R = 1$ .

Table 1 shows that all solvers recover a stencil very close to the exact centered difference. In Figures 1 and 2 we compare the space–time evolution and the final-time profile of the electric field  $E(x, t)$  for each learned stencil against the reference FD solution. The space–time plots in Figure 1 show that the learned stencils reproduce essentially the same wave propagation as the exact centered difference, while the final-time profiles in Figure 2 are visually indistinguishable from the reference solution.

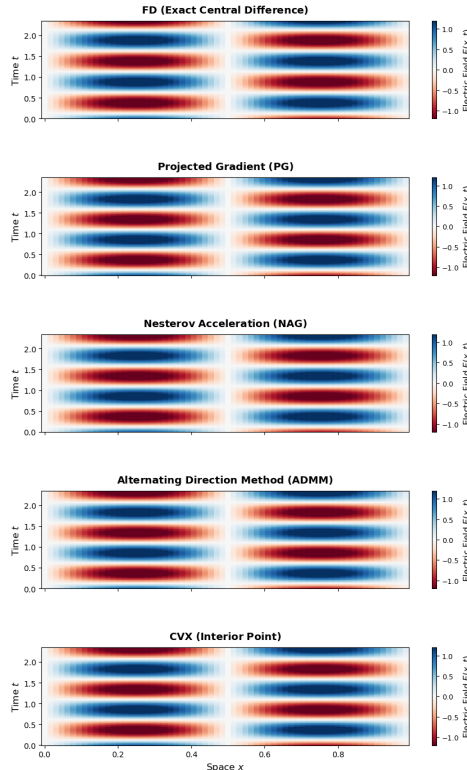


Figure 1: Space–time evolution of the electric field  $E(x, t)$  for the reference central-difference stencil and the learned stencils with radius  $R = 1$ . Each panel shows  $E(x, t)$  over the full simulation time.

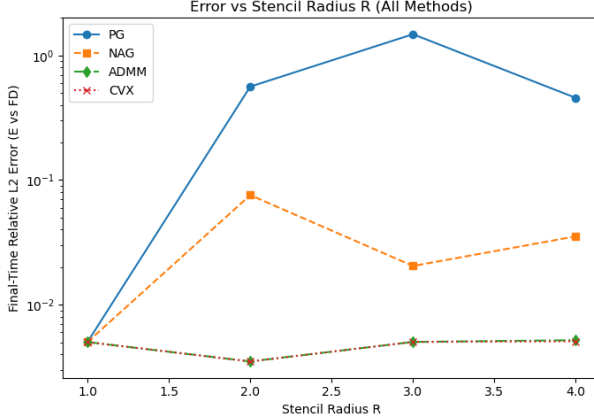


Figure 3: Final-time relative  $L^2$  error in the electric field versus stencil radius  $R$  for each solver, using Crank–Nicolson time integration.

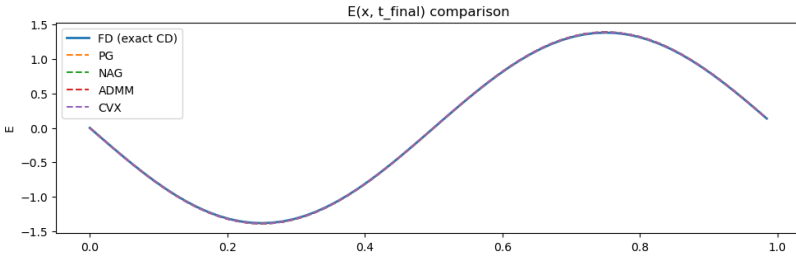


Figure 2: Final-time electric field  $E(x, T)$  for the exact central-difference stencil and the learned stencils for  $R = 1$  under Crank–Nicolson time-stepping. The curves are visually indistinguishable at the scale shown.

### 6.3 Error and energy residual versus stencil radius

To explore the effect of stencil size, we repeat the learning and time-integration procedure for radii  $R = 1, 2, 3, 4$ . Figure 3 shows the final-time relative  $L^2$  error  $\text{err}(w)$  for each method as a function of  $R$ .

Figure 3 shows that for  $R = 1$  all four solvers achieve comparable accuracy, with errors on the order of  $5 \times 10^{-3}$ . As the radius increases, the behavior diverges: the projected-gradient and Nesterov methods exhibit substantially larger errors, with PG reaching  $\mathcal{O}(1)$  error and NAG reaching  $\mathcal{O}(10^{-2})$  for  $R = 3$ . In contrast, the ADMM and CVX solutions maintain errors in a narrow band between approximately  $3 \times 10^{-3}$  and  $6 \times 10^{-3}$  for all radii tested. This indicates that the second-order KKT solve in ADMM and the interior-point method in CVX are more effective at exploiting the additional degrees of freedom introduced by larger stencils, whereas the first-order projected methods struggle to fully optimize the objective within the available iteration budget.

### 6.4 Discrete energy conservation for learned Maxwell stencils

We next examine how closely the learned stencils preserve the semi-discrete electromagnetic energy under Crank–Nicolson time integration.

Figure 4 compares the discrete electromagnetic energy error  $\mathcal{E}^n - \mathcal{E}^0$  for Crank–Nicolson time integration using the exact central-difference stencil and the structure-preserving learned stencils.

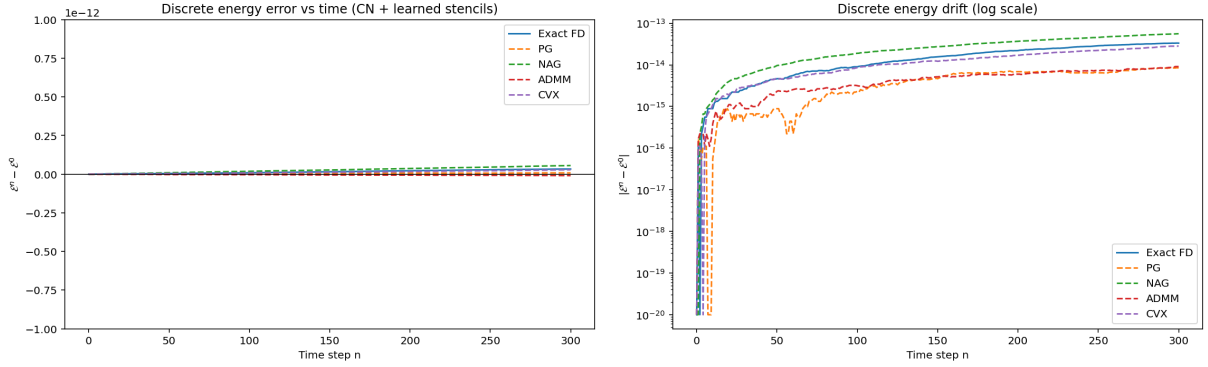


Figure 4: Discrete energy error  $\mathcal{E}^n - \mathcal{E}^0$  for Crank–Nicolson time stepping with the exact central-difference stencil and the structure-preserving learned stencils, shown on a linear (left) and logarithmic (right) scale.

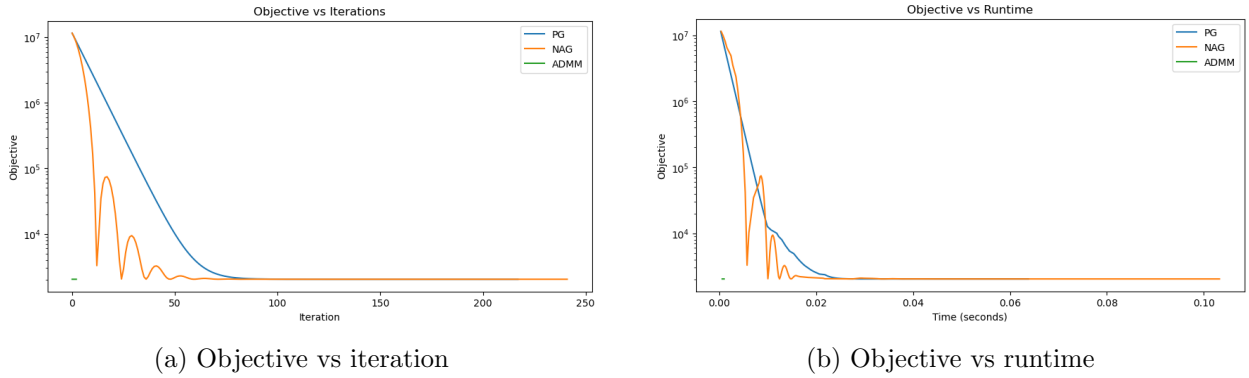


Figure 5: Convergence behavior of PG, NAG, and ADMM for a fixed stencil radius  $R$ . Left: objective value versus iteration count. Right: objective value versus wall-clock runtime.

On the linear scale, all curves are essentially flat and remain at the level of  $10^{-12}$ , indicating that the total energy is conserved up to machine precision for all methods. The logarithmic view reveals small differences: the PG, ADMM, and CVX stencils produce energy drift of the same order as the exact FD stencil, while NAG exhibits a slightly larger but still very small drift. These results confirm that enforcing the skew-symmetry constraints during training yields learned stencils that are effectively energy-preserving under Crank–Nicolson time stepping.

## 6.5 Solver convergence and runtime

Finally, we compare the convergence histories of the different solvers. Figure 5a plots the objective value versus iteration for each first-order method for a fixed radius. Figure 5b shows the same objective versus wall-clock time. These plots illustrate the tradeoffs among PG, NAG, and ADMM in terms of iterations, per-iteration cost, and constraint enforcement.

Figure 5a shows that all three methods reduce the objective by several orders of magnitude, but their convergence patterns differ. PG exhibits the expected monotone, roughly geometric decrease. NAG achieves a much faster reduction in the first  $\sim 20$  iterations, but with the characteristic oscillations of accelerated gradient methods before settling near the optimum. ADMM appears as an almost flat curve at the bottom of the plot because it solves a small KKT system at each

iteration; in this setting, one or two ADMM iterations are enough to reach an objective value comparable to the final PG/NAG iterates.

Figure 5b plots the same objective values against wall-clock time. Because PG and NAG have very cheap iterations, their curves almost coincide and reach a low objective well below  $10^{-3}$  in about  $10^{-2}$  seconds for our problem size. ADMM has a higher per-iteration cost due to the linear solve, but it reaches essentially its final objective in a single step, so the total runtime is competitive with the first-order methods in this regime. For larger-scale problems, we expect the trade-off between cheap but many iterations (PG/NAG) and expensive but very few iterations (ADMM) to be even more pronounced.

## 7 Conclusion

We proposed an energy-conserving, data-driven discretization framework for the one-dimensional Maxwell system. By learning convolution stencils from spectral training data under a linear skew-symmetry constraint, we obtain discrete derivative operators that are guaranteed to be skew-adjoint and therefore exactly conserve semi-discrete electromagnetic energy. Numerical experiments show that the resulting schemes match the accuracy of standard central differences while preserving these structural properties. Using Crank–Nicolson time integration, we further confirmed that the discrete energy remains constant to roundoff for learned stencils satisfying the skew-adjoint constraint.

## 8 Discussion and extensions

The experiments above illustrate that simple linear constraints can encode important structural information in data-driven discretizations of PDEs. In this setting, the skew-symmetry constraint  $Cw = d$  ensures semi-discrete energy conservation and leads to stencils that behave like standard centered differences but are obtained purely from data.

Future work will learn staggered curl operators that preserve a discrete Poynting theorem in 2D/3D, integrate material models (Lorentz/Duffing) with structure-preserving polarization updates, and incorporate boundary treatments (ABC/CPML). On the optimization side, extending the comparison to higher-order stencils, non-quadratic objectives, and learned nonlinear fluxes would help clarify the regimes in which ADMM or interior-point methods offer the best tradeoff relative to accelerated first-order algorithms. Ultimately, combining learning with physics-motivated constraints promises accurate, stable reduced models for large-scale CEM while keeping the mathematical guarantees that make FDTD dependable [15, 5].

## References

- [1] J. Bar-Sinai, S. Hoyer, J. Hickey, and M. Levine. Learning data-driven discretizations for partial differential equations. *Proceedings of the National Academy of Sciences*, 116(31):15344–15349, 2019.
- [2] Vrushali A. Bokil, Olivia A. Keefer, and Amy C.-Y. Leung. Operator splitting methods for maxwell’s equations in dispersive media with orientational polarization. *Journal of Computational and Applied Mathematics*, 263:160–188, 2014.

- [3] J. Crank and P. Nicolson. A practical method for numerical evaluation of solutions of partial differential equations of the heat-conduction type. *Proceedings of the Cambridge Philosophical Society*, 43(1):50–67, 1947.
- [4] Michael B. Giles. Crank–nicolson time-marching. Lecture notes, University of Oxford, 2010.
- [5] Ernst Hairer, Christian Lubich, and Gerhard Wanner. *Geometric Numerical Integration: Structure-Preserving Algorithms for Ordinary Differential Equations*, volume 31 of *Springer Series in Computational Mathematics*. Springer, 2nd edition, 2006.
- [6] Ernst Hairer and Gerhard Wanner. *Solving Ordinary Differential Equations II: Stiff and Differential-Algebraic Problems*, volume 14 of *Springer Series in Computational Mathematics*. Springer, 2 edition, 2010.
- [7] Dmitrii Kochkov, Jamie A. Smith, Ayya Alieva, Qing Wang, Michael P. Brenner, and Stephan Hoyer. Machine learning–accelerated computational fluid dynamics. *Proceedings of the National Academy of Sciences*, 118(21):e2101784118, 2021.
- [8] Randall J. LeVeque. *Finite Difference Methods for Ordinary and Partial Differential Equations*. Society for Industrial and Applied Mathematics, 2007.
- [9] Julia Ling, Andrew Kurzawski, and Jeremy Templeton. Reynolds averaged turbulence modelling using deep neural networks with embedded invariance. *Journal of Fluid Mechanics*, 807:155–166, 2016.
- [10] K. W. Morton and D. F. Mayers. *Numerical Solution of Partial Differential Equations: An Introduction*. Cambridge University Press, 1994.
- [11] Eric J. Parish and Karthik Duraisamy. A paradigm for data-driven predictive modeling using field inversion and machine learning. *Journal of Computational Physics*, 305:758–774, 2016.
- [12] Maziar Raissi, Paris Perdikaris, and George E. Karniadakis. Hidden physics models: Machine learning of nonlinear partial differential equations. *Journal of Computational Physics*, 357:125–141, 2018.
- [13] R. D. Richtmyer and K. W. Morton. *Difference Methods for Initial-Value Problems*. Wiley-Interscience, 2 edition, 1967.
- [14] Samuel H. Rudy, Steven L. Brunton, Joshua L. Proctor, and J. Nathan Kutz. Data-driven discovery of partial differential equations. *Science Advances*, 3(4):e1602614, 2017.
- [15] Allen Taflove and Susan C. Hagness. *Computational Electrodynamics: The Finite-Difference Time-Domain Method*. Artech House, 3rd edition, 2005.